ISSN (Print) 1226-1750
ISSN (Online) 2233-6656
Journal of Magnetics 30(4), 489-497 (2025) https://doi.org/10.4283/JMAG.2025.30.4.489

Stoichiometry-Controlled Coprecipitation Synthesis of Single-Phase Sr–Ni W-type Ferrite for Electromagnetic Wave Absorption

Changjin Jung[1,2], Byeongjin Park[2], Je In Lee[1]*, and Horim Lee[2]*

[1]*School of Materials Science and Engineering, Pusan National University, 2 Busandaehak-ro 63beon-gil, Geumjeong-gu, Busan 46241, Republic of Korea*
[2]*Korea Institute of Materials Science, 797 Changwonadero, Seongsan-gu, Changwon, Gyeongnam 51508, Republic of Korea*

(Received 22 September 2025, Received in final form 11 December 2025, Accepted 11 December 2025)

Optimized synthesis conditions for single-phase Sr–Ni W-type ferrite were established via a Na_2CO_3-assisted coprecipitation route. A NaOH-Na_2CO_3 mixed precipitant and calcination at 1250 °C produced single-phase W-type ferrite by preventing Sr loss during washing. The optimized W-type ferrite powders were incorporated into a thermoplastic polyurethane (TPU) matrix to fabricate thin, flexible composites. Electromagnetic characterization indicates dominant ferromagnetic resonance (FMR)-driven magnetic loss; transmission-line based reflection loss (RL) calculations predict a broad effective absorption bandwidth (EAB) of 9.3 GHz (40.9–50.2 GHz) at a thickness of 0.65 mm, with RL_{min} below –40 dB. These findings demonstrate that Na_2CO_3-mediated precursor control enables reproducible single-phase W-type ferrite and yields high-performance electromagnetic wave absorbers for mm-wave applications.

Keywords : hexaferrite, coprecipitation, ferromagnetic resonance, electromagnetic absorbers

1. Introduction

The rapid advancement of 5G and next-generation 6G communication technologies has expanded the operating frequencies of electronic devices from below 3 GHz to well above 30 GHz. In particular, various high-frequency technologies such as autonomous vehicle radar systems (24, 77 GHz), satellite communications, and high-speed wireless internet have become commercialized, making the use of high-frequency electromagnetic wave (EM wave) essential [1-4]. While this shift toward higher frequencies provides advantages like high-speed communication and large-volume data transmission, it also raises concerns about electromagnetic interference (EMI) among electronic devices, amplifying EMI-related issues [4]. For instance, EMI within autonomous vehicles can lead to radar signal distortion or malfunctions, potentially causing critical safety problems, while performance degradation can also occur between semiconductor components.

One of the primary approaches to address such high-frequency EMI problems is the development of EM wave absorbers. Traditionally, reflective shielding materials based on highly conductive materials like metals, carbon, and MXenes have been predominantly used. Although such materials provide excellent shielding efficiency, their reflective nature can generate secondary interference in adjacent circuits [5, 6]. Consequently, attention has shifted toward absorption-based materials that dissipate electromagnetic energy into thermal energy. Absorption-based shielding relies on dielectric and magnetic losses, with ferromagnetic resonance (FMR) serving as the dominant magnetic loss mechanism in the GHz range. From this perspective, hexagonal ferrites have attracted significant attention as EM wave absorbers due to their excellent magnetic properties in GHz bands, thermal stability, and low conductivity [7]. Particularly, hexaferrites can induce FMR in the tens-of-gigahertz range due to their high magnetic anisotropy fields, making them ideal candidates for mm-wave absorbers.

Among hexaferrites, W-type ferrites have emerged as promising alternatives. W-type ferrites exhibit high magnetic anisotropy fields, positioning the FMR frequency about 40 GHz and enabling coverage from X-band to Ka-band frequency ranges [8]. Structurally, W-

---

*Co-corresponding author: Tel: +82-55-280-3138
Fax: +82-55-280-3498, E-mail: jilee@pusan.ac.kr (J.I. Lee)
E-mail: horimlee@kims.re.kr (H. Lee)

type ferrite adopts an M+2S structure with two additional spinel blocks (S-blocks) added to the M-type structure. This structure provides additional M^{2+} sites that facilitate transition-metal substitution, offering greater compositional flexibility [9, 10]. Despite these advantages, synthesizing single-phase W-type ferrites is experimentally challenging due to their structural complexity and the high energy barrier for crystallization [11]. Typically, single-phase W-type ferrites require calcination above 1300 °C, and in Sr- or Ba-based systems, precise stoichiometric control is essential [12]. Failure to control stoichiometry often results in mixed phase powder containing spinel or M-type ferrites, which compromise magnetic performance and reproducibility [10, 13-15]. Previous researches still fall short of providing a simple, mass-producible synthesis route for the stable production of single-phase W-type ferrite [9, 15-17].

In this work, we targeted single-phase synthesis of Sr–Ni W-type ferrite via a coprecipitation route. Previous coprecipitation studies commonly used NaOH as the sole precipitant, causing Sr to precipitate as relatively soluble $Sr(OH)_2$ ($K_{sp} \approx 3.2\times10^{-4}$ at 25 °C) and leading to Sr loss during washing; consequently, excess Sr addition was often required to obtain single-phase products [14, 18, 19]. To avoid this problem, we introduce Na_2CO_3 to drive Sr precipitation as sparingly soluble $SrCO_3$ ($K_{sp} \approx 5.6\times 10^{-10}$ at 25 °C), which stabilizes Sr content in the precursor and preserves near-stoichiometric compositions that favor W-type phase formation.

Furthermore, we systematically investigated phase formation and magnetic properties as a function of calcination temperature (1100-1300 °C) and incorporated the optimized powders into a thermoplastic polyurethane (TPU) matrix to fabricate thin, flexible EM wave absorbers. Measured complex permittivity and permeability indicate dominant magnetic loss from FMR, and transmission-line based RL calculations yield a broad effective absorption bandwidth (EAB) of 9.3 GHz at a thickness of 0.65 mm. These results demonstrate the promise of Sr–Ni W-type ferrite/TPU composites as lightweight, high-performance absorbers for next-generation high-frequency applications.

2. Experimental

2.1. Materials

To synthesize Sr–Ni W-type ferrites, strontium nitrate ($Sr(NO_3)_2$), iron(III) nitrate nonahydrate ($Fe(NO_3)_3\cdot9H_2O$), and nickel(II) nitrate hexahydrate ($Ni(NO_3)_2\cdot6H_2O$) were used as precursor materials for precipitation. Sodium hydroxide (NaOH) and sodium carbonate (Na_2CO_3) were employed as precipitants. All reagents were supplied by Sigma-Aldrich (USA) and used as received, without any additional purification. For the fabrication of EM wave absorbing composites, a thermoplastic polyurethane (TPU) binder solution containing 30 wt% TPU dissolved in a mixed solvent of N,N-dimethylformamide (DMF) and methyl ethyl ketone (MEK) was utilized. The TPU

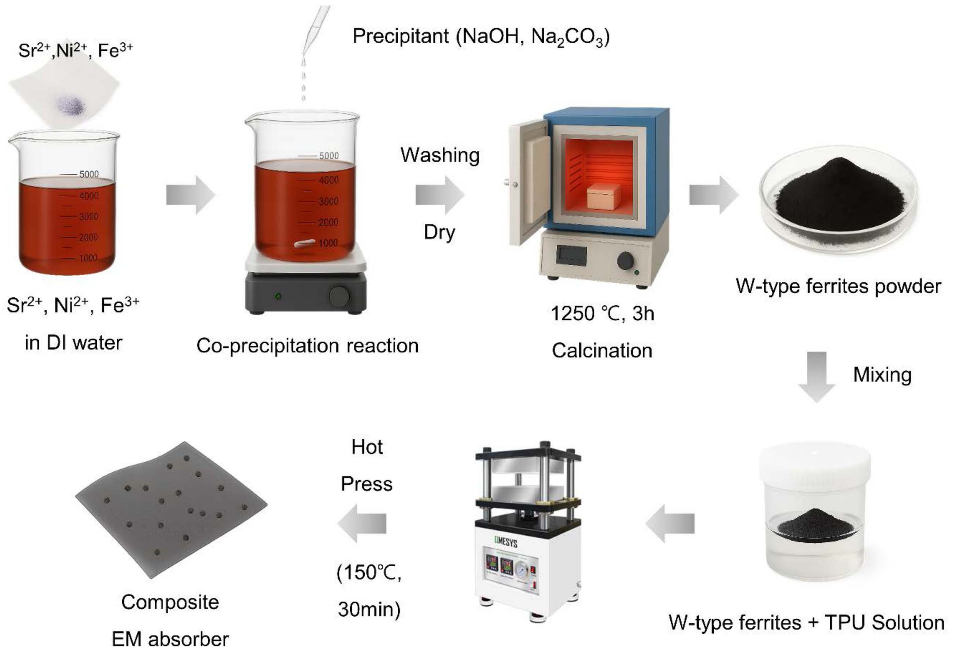

Fig. 1. (Color online) Schematic illustration of the Sr–Ni W-type ferrite powder via coprecipitation method and the composite process for EM wave absorber.

solution was obtained from Songwon Industrial (Korea).

2.2. Synthesis of Sr–Ni W-type ferrite powder

Sr–Ni W-type ferrite powders with the nominal composition of $SrNi_2Fe_{16}O_{27}$ were prepared via a conventional coprecipitation route. The overall synthesis procedure is schematically illustrated in Fig. 1. Stoichiometric amounts of strontium nitrate ($Sr(NO_3)_2$), iron(III) nitrate nonahydrate ($Fe(NO_3)_3 \cdot 9H_2O$), and nickel(II) nitrate hexahydrate ($Ni(NO_3)_2 \cdot 6H_2O$) were dissolved in deionized (DI) water, with the Sr^{2+} concentration fixed at 0.05 M. Three types of alkaline precipitating agents were utilized: a single NaOH solution and a mixed alkaline solution composed of NaOH and Na_2CO_3 in a 10:1 molar ratio, with final concentrations adjusted to 2 M or 4 M. The alkaline solution was slowly added to the metal nitrate solution under constant stirring until the pH reached 11, leading to the formation of precursor precipitates. The resulting precipitates were thoroughly washed with DI water until the solution reached a neutral pH (~7), then dried in a convection oven (JSOF-100P, JSR, Korea). Afterward, the dried powders were manually ground, calcined at 1100, 1200, 1250, or 1300 °C for 3 hours, and finally re-ground into fine ferrite powders.

2.3. Preparation of the Sr–Ni W-type ferrite EM wave absorber

The prepared Sr–Ni W-type ferrite powders and the TPU solution were uniformly mixed at a weight ratio of 4:6, 3:7, 2:8 (TPU:ferrite). The mixing was conducted in a planetary mixer (ARE-310, THINKY, Japan) under conditions of 2000 rpm for 3 min for homogenization, followed by a defoaming step at 2200 rpm for 2 min. The homogeneously mixed slurry was then cast into films using a doctor blade (TO-500, Automatic Control Coater, Korea) to control the thickness of the composite layer. Subsequently, the cast films were dried at 110 °C for 2 hours in a convection oven to fully remove residual DMF and MEK solvents. Finally, the dried films were thermally pressed at 150 °C under a pressure of 5 MPa for 30 min to obtain composite absorbers suitable for EM wave absorption testing.

2.4. Characterization

The surface morphologies of the Sr–Ni W-type ferrite powders were characterized using scanning electron microscopy (SEM; JSM-7001F, JEOL, Japan). Crystal structural properties were identified by X-ray diffraction analysis (XRD; SmartLab XE (9kW), RIGAKU, Japan) utilizing Cu Kα radiation. The magnetic properties of the synthesized ferrite powders were analyzed by measuring magnetic hysteresis loops with a vibrating sample magnetometer (VSM; EZ9, MicroSense, USA) under an applied magnetic field of ±25 kOe. Additionally, the complex permittivity and permeability of the composite samples were evaluated using a vector network analyzer (VNA; N5291A, Keysight, USA) in the frequency range of 33-60 GHz.

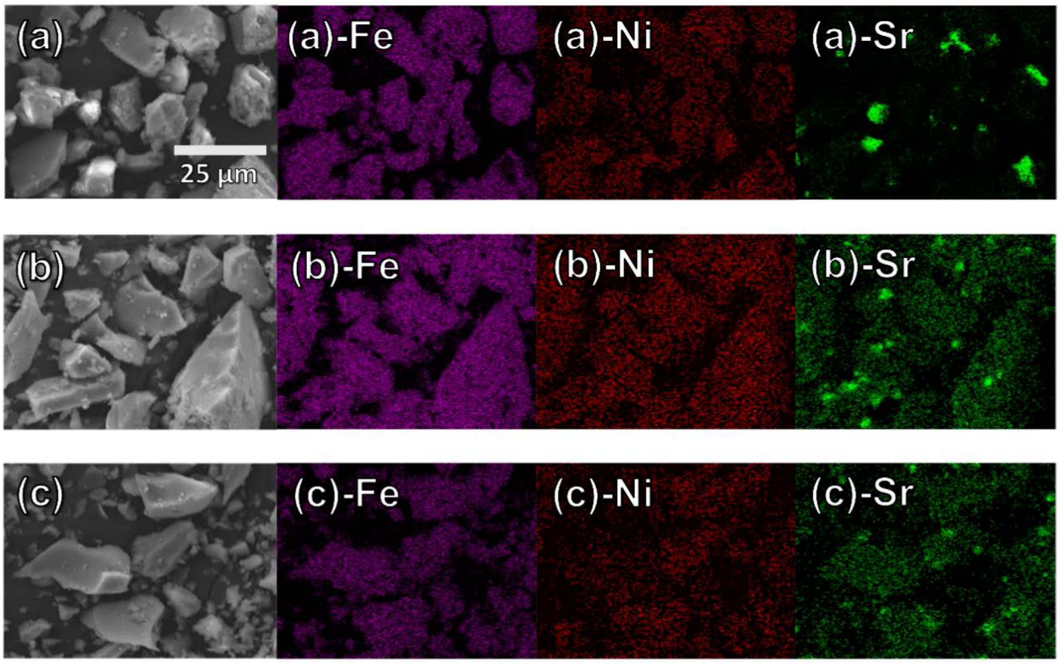

Fig. 2. (Color online) Elemental mappings images of precursors (a) Sample A, (b) Sample B, (c) Sample C.

3. Results and Discussion

3.1. Effect of Sodium Carbonate on the as-precipitated precursor stoichiometry

Fig. 2 presents the scanning electron microscopy-energy dispersive spectroscopy (SEM–EDS) elemental mapping results of precursor powders synthesized under different precipitant conditions, in order to examine whether the nominal stoichiometry of the precipitated precursor was preserved. Since the synthesis of precursors with accurate stoichiometric ratios is crucial for obtaining single-phase Sr–Ni W-type ferrites, the selection of an appropriate precipitant is a critical factor [10, 15, 20, 21]. To minimize Sr^{2+} loss and maintain accurate stoichiometric ratios, Sr^{2+} should be precipitated in the form of low-solubility carbonate, rather than hydroxide. To verify the influence of carbonate in precipitant on the stoichiometry, precursors were precipitated using three different precipitant solutions: Sample A (precipitated by 4 M NaOH), Sample B (precipitated by 2 M NaOH-Na_2CO_3 mixed solution, molar ratio 10:1), and Sample C (precipitated by 4 M NaOH-Na_2CO_3 mixed solution, molar ratio 10:1). Fig. 2(a), 2(b), and 2(c) shows the Sample A, Sample B and C, respectively. The 10:1 molar ratio was based on a stoichiometric analysis of the $SrNi_2Fe_{16}O_{27}$ target. Theoretically, precipitating the desired $SrCO_3$, $Ni(OH)_2$, and $Fe(OH)_3$ requires a 1 CO_3^{2-} to 52 OH^- ionic ratio (from (2×2) + (16×3)), corresponding to a minimum NaOH:Na_2CO_3 ratio of 52:1. Our 10:1 ratio, therefore, provided a significant excess of Na_2CO_3. This intentional excess was designed to suppress the competing formation of soluble $Sr(OH)_2$ ($K_{sp} \approx 3.2\times10^{-4}$) and decisively favor the precipitation of highly insoluble $SrCO_3$ ($K_{sp} \approx 5.6 \times10^{-10}$), ensuring complete Sr capture. Thus, the 10:1 ratio was selected as a sufficient condition to guarantee the stoichiometric stability of the precursor.

As shown in Fig. 2(a), Sr^{2+} exhibits localized aggregation in specific regions, indicating non-uniform dispersion of Sr^{2+} during the precipitation process. In contrast, Fe and Ni were uniformly distributed throughout the area. This inhomogeneous distribution of Sr^{2+} can be attributed to the loss of water–soluble $Sr(OH)_2$ after washing with DI water. On the other hand, as presented in Fig. 2(b) and 2(c), samples prepared using mixed solutions with Na_2CO_3 showed a homogeneous distribution of all elements, with no evidence of localized concentration. This homogeneity is attributed to the formation of poorly soluble $SrCO_3$, which immobilizes Sr^{2+} within the precursor and prevents leaching during washing.

The atomic-ratio analysis (Table 1) further corroborates these observations: samples precipitated from mixed-precipitant solutions containing Na_2CO_3 exhibited atomic ratios close to the nominal Sr:Ni:Fe = 1:2:16 composition, consistent with the ideal W-type ferrite stoichiometry. By contrast, samples precipitated using a single NaOH solution showed reduced Sr^{2+} content, indicating compositional deviation likely caused by Sr^{2+} loss during washing. Therefore, precipitation with mixed-precipitant solutions that include Na_2CO_3 is necessary to obtain Sr–Ni W-type ferrite precursors whose nominal and experimental compositions agree; this approach minimizes Sr leaching by controlling the precipitation form of Sr^{2+} and thereby improves compositional stability.

Table 1. Nominal compositions and atomic ratios of precursor powders calculated from EDS data.

		Sr (at %)	Ni (at %)	Fe (at %)
Nominal Composition	atomic ratio	1	2	16
Sample A	measured atomic ratio	1	2.36	29.44
Sample B	measured atomic ratio	1	1.90	15.51
Sample C	measured atomic ratio	1	2.04	16.63

3.2. Effect of Sodium Carbonate on Phase and Microstructure of Sr–Ni W-type Ferrites

To evaluate the effect of Sodium Carbonate on the morphology of calcined W-type ferrite powders, dried precursor powders were calcined at 1250 °C for 3 hours and their microstructures were analyzed by SEM. The results are presented in Fig. 3. As shown in Fig. 3(a), the powder synthesized with Sample A exhibited relatively large particles, and some particles formed tetrahedral morphologies characteristic of spinel phase crystal structures [22]. These morphologies are attributed to Sr deficiency concluded by earlier EDS analysis, which favored the formation of spinel ferrite phases rather than W-type ferrite [15].

In contrast, samples synthesized with Sample B and C (Fig. 3(b) and 3(c)) clearly displayed hexagonal platelet morphologies with particle sizes of approximately 5-10 μm. The inset images show well-defined hexagonal facets, consistent with hexagonal crystal growth and indicating successful formation of W-type ferrite due to preserved stoichiometric Sr content in the precursors. Moreover, no significant differences in particle size or morphology were observed between calcined particles by Sample B and C. This suggests that at Na_2CO_3 concentrations over 2 M, Sr^{2+} is effectively precipitated as $SrCO_3$,

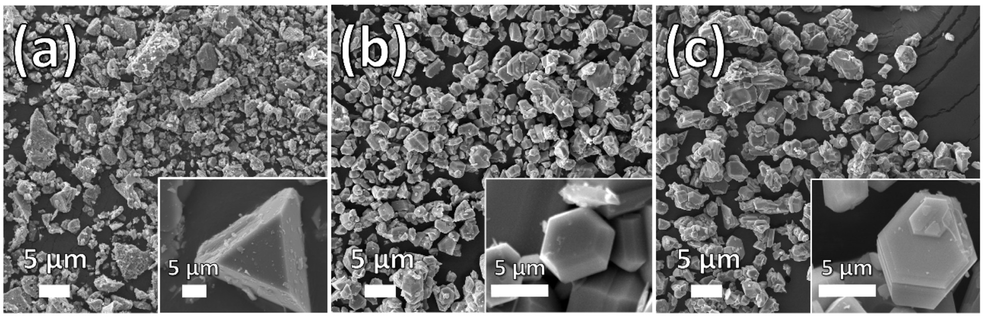

Fig. 3. SEM images of Sr–Ni W-type ferrites using (a) Sample A, (b) Sample B, (c) Sample C.

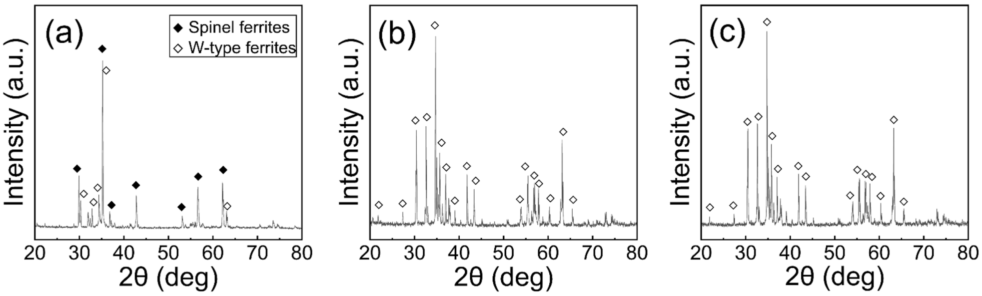

Fig. 4. XRD patterns of Sr–Ni W-type ferrites using (a) Sample A, (b) Sample B, (c) Sample C.

and thus stoichiometry is maintained during subsequent processing.

The crystal structure and phase composition of the synthesized Sr–Ni W-type ferrite powders were investigated using X-ray diffraction (XRD), with the results shown in Fig. 4. W-type ferrite is known to crystallize in the hexagonal $P6_3/mmc$ space group. The XRD patterns of Samples (b) and (c) match the standard pattern for W-type ferrite, confirming their single-phase nature (Fig. 4(b) and 4(c)) [23].

In contrast, the pattern for Sample (a) in Fig. 4(a) exhibits weak diffraction peaks from the W-type ferrite phase, alongside much stronger peaks attributed to secondary spinel ferrite [24]. This suggests that the partial loss of Sr^{2+} during synthesis processing hindered the formation of W-type ferrite, causing the residual Fe ions to preferentially form the more stable spinel structure. These findings are consistent with the previous SEM and EDS analyses and confirm that using Na_2CO_3 as a precipitant stabilizes stoichiometry, leading to the successful formation of a single-phase W-type ferrite structure.

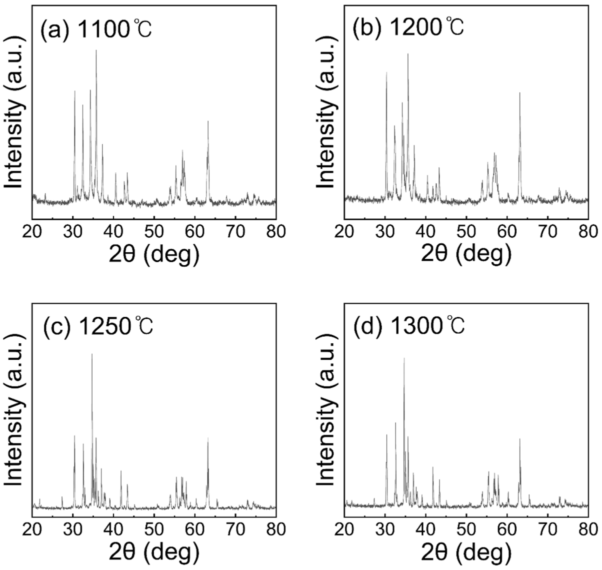

Fig. 5. XRD patterns of Sr–Ni W-type ferrites calcined at different temperatures (a) 1100 °C, (b) 1200 °C, (c) 1250 °C, and (d) 1300 °C.

3.3. Effect of calcination temperature

Based on the previous analyses, it was confirmed that a precipitant containing NaOH and Na_2CO_3 (at concentrations above 2 M) provides effective conditions for the single-phase synthesis of Sr–Ni W-type ferrites. Accordingly, to investigate the phase evolution and magnetic properties as a function of calcination temperature, Sample C was calcined at 1100, 1200, 1250, and 1300 °C for 3 hours. The resulting powders were then analyzed by XRD (Fig. 5).

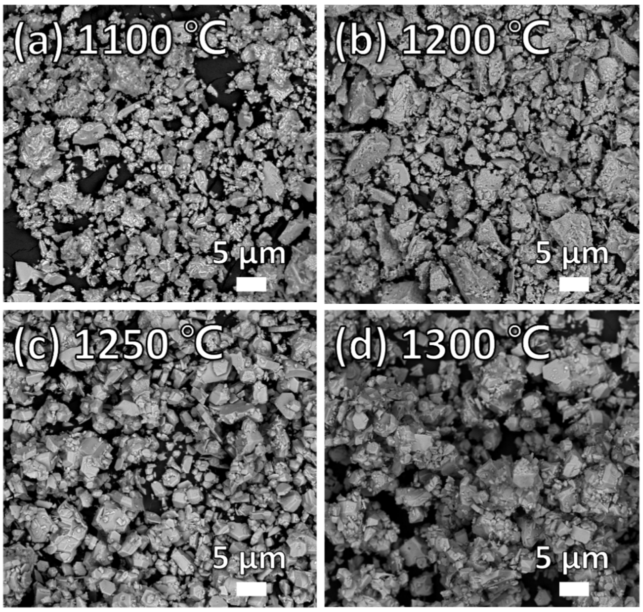

Fig. 6. SEM images of Sr–Ni W-type ferrites at different calcination temperatures (a) 1100 °C, (b) 1200 °C, (c) 1250 °C, and (d) 1300 °C.

The XRD patterns for the samples calcined at 1100 and 1200 °C (Fig. 5(a) and 5(b)) did not show distinct peaks corresponding to W-type ferrite; instead, peaks from the M-type ferrite phase were dominant [25, 26]. This indicates that the phase transformation was incomplete at these temperatures, with the calcined powder remaining in an intermediate M-type phase due to insufficient thermal energy to overcome the activation barrier for crystal growth [11-13]. The broad peak widths of these samples also suggest poor crystallinity.

In contrast, at temperatures of 1250 °C and higher, sharp diffraction peaks for W-type ferrite were clearly observed, while most of the M-type phase had disappeared. This indicates that the W-type phase becomes stable and the transformation to a single-phase structure is completed above 1250 °C.

Fig. 6 presents SEM images used to examine the particle size and morphology of the powders calcined at different temperatures. While the samples calcined at 1100, 1250, and 1300 °C exhibited similar particle sizes, the sample calcined at 1200 °C displayed abnormally large grains exceeding 10 μm. Consistent with the XRD results, this abnormal grain growth is attributed to the presence of the M-type ferrite phase, which promoted rapid grain coarsening at higher temperature of 1200 °C than 1100 °C [25, 26]. In contrast, at temperatures of 1250 °C and above, the formation of a stable W-type phase suppressed this effect, maintaining particle sizes within the 5-10 μm range.

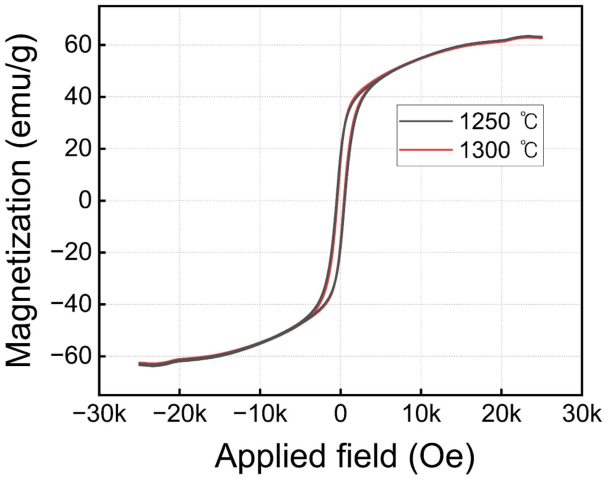

Fig. 7. (Color online) Magnetic hysteresis loop of Sr–Ni W-type ferrites.

At lower temperatures (≤1200 °C), insufficient thermal energy led to the coexistence of M-type and other phases, even though the nominal precursor composition was for W-type ferrite. Consequently, the characteristic hexagonal structures of hexaferrite were only sparsely observed. At higher calcination temperatures (≥1250 °C), however, the W-type phase was fully stabilized, and well-defined hexagonal platelets were clearly visible.

3.4. Magnetic properties of Sr-Ni W-type ferrites

The magnetic properties of the calcined Sr–Ni W-type ferrite powders were characterized at room temperature using a VSM, with the resulting M-H loops and detailed parameters are presented in Fig. 7 and Table 2, respectively. All Sr–Ni W-type ferrite samples exhibited smooth, S-shaped M-H curves without kinks or steps, which indicates the absence of magnetically distinct secondary phases.

The high magnetization values for the Sr–Ni W-type ferrite powder calcined at 1250 °C (63.6 emu/g) and 1300 °C (63.3 emu/g) are consistent with those previously reported for single-phase W-type ferrites [9, 11, 27]. Their low coercivity further confirms their soft magnetic behavior. The slight decrease in coercivity from the 1250 °C to the 1300 °C calcined powder is attributed to

Table 2. The magnetization at 25 kOe ($M_{s(25kOe)}$) and Coercive field (H_c) values of the Sr–Ni W-type ferrites.

Temperature	$M_{s(25kOe)}$ (emu/g)	H_c (Oe)
1250 °C	63.568	503.364
1300 °C	63.264	415.122

increased grain size, a common phenomenon in soft magnetic ferrites [26, 28].

Combining the structural (XRD), morphological (SEM), and magnetic (VSM) results, we determined that 1250 °C is the minimum temperature required to synthesize single phase Sr–Ni W-type ferrite. To balance the need for phase purity with energy efficiency and cost, 1250 °C is proposed as the optimal calcination temperature for this Sr–Ni W-type ferrite synthesis system.

3.5. Electromagnetic properties of Sr–Ni W-type ferrite composites

Based on the previous analyses, Sr–Ni W-type ferrite powders were synthesized using precipitant of Sample C and calcined at 1250 °C for 3 hours. To evaluate the electromagnetic properties of synthesized Sr–Ni W-type ferrite, composite films were prepared by embedding the Sr–Ni W-type ferrite powders in a TPU matrix with three different fractions (60, 70, and 80 wt%). The complex permittivity (ε_r) and permeability (μ_r) of the composite films were measured using a VNA, with the results presented in Fig. 8(a) and 8(b), respectively. The solid lines and dashed lines indicate the real part and imaginary part of complex permittivity and complex permeability, respectively.

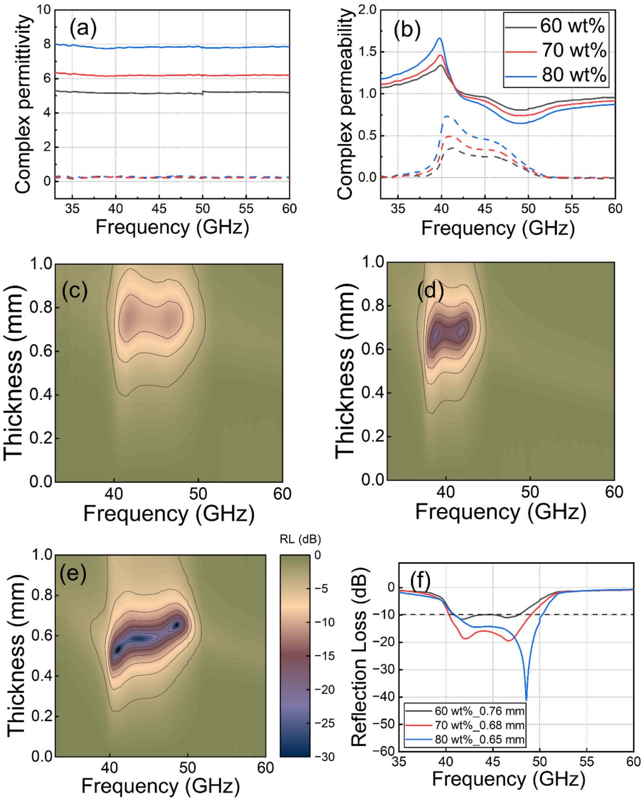

Fig. 8. (Color online) (a) complex permittivity and (b) complex permeability of the Sr–Ni W-type ferrite absorbers (c–e) 2D contour plots of RL values for Sr–Ni ferrites contents (c) 60 wt%, (d) 70 wt% and (e) 80 wt% (f) calculated RL of the absorbers.

As shown in Fig. 8(a), the real and imaginary parts of the permittivity are nearly constant across the measured frequency range. It was confirmed that as the content of the Sr–Ni W-type ferrite powder increases, the real part of the permittivity increases from approximately 5.1 (at 60 wt%) to 7.8 (at 80 wt%). However, the imaginary part of the permittivity shows a low value below 0.3 regardless of the ferrite content, confirming that there is minimal dielectric loss. In the case of permeability, unlike permittivity, a peak caused by ferromagnetic resonance (FMR) was observed between 36 and 52 GHz. Furthermore, as the ferrite powder content increased, it was confirmed that the real and imaginary parts of the permeability increased concurrently, leading to an increase in magnetic loss.

The EM wave absorption performance of the TPU/W-type ferrite composite absorbers backed with a perfect electric conductor (PEC) was evaluated by calculating the reflection loss (RL) using transmission line theory. [25] The input impedance (Z_{in}) of the absorber was determined by the following equation:

$$Z_{in} = Z_0 \sqrt{\frac{\mu_r}{\varepsilon_r}} tanh\left(\frac{2j\pi f d}{c}\sqrt{\mu_r \varepsilon_r}\right) \tag{1}$$

$$RL(dB) = 20log\left|\frac{z-1}{z+1}\right| \tag{2}$$

where Z_0 represents the electromagnetic characteristic impedance of free space, f is the frequency, d is the sample thickness, and c is the speed of light. Fig. 8(c), 8(d) and 8(e) present the two-dimensional (2D) contour plots of RL values, which were calculated from the measured complex permittivity and permeability according to Equations (1) and (2). All three absorbers exhibited low RL values in the frequency ranges corresponding to the FMR, which show strong magnetic loss. However, the minimum RL value and absorption bandwidth differ depending on the W-type ferrite content. As the W-type ferrite content increased, the effective absorption bandwidth (EAB) broadened, and the matching thickness required to achieve the minimum RL decreased. As shown in Fig. 8(f), the 80 wt% composite demonstrated the broadest EAB, confirming its superior absorption performance even at a reduced thickness. The optimized matching thickness, EAB, and RL_{min} values for different ferrite contents are summarized in Table 3.

Table 3. Summary of electromagnetic absorption performance of absorbers.

Contents of W-type ferrite (wt %)	Thickness (mm)	EAB (GHz)	RL_{min} (dB)
60	0.76	2.72, 2.47	–11.6
70	0.68	8.7	–19.5
80	0.65	9.3	–41.3

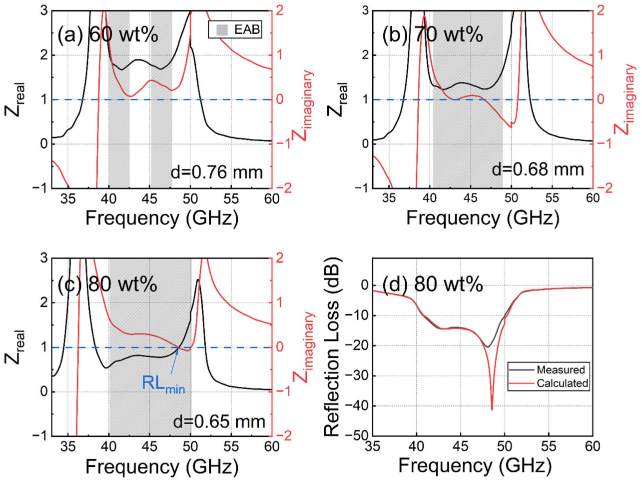

Fig. 9. (Color online) Real and imaginary parts of the normalized input impedance (Z) for Sr–Ni ferrite absorbers with different ferrite contents: (a) 60 wt%, (b) 70 wt%, (c) 80 wt%. (d) comparison of the measured and calculated RL values for 80 wt% absorber.

The normalized input impedance Z (defined as Z_{in}/Z_0), calculated from the measured material properties, is a critical parameter for absorber performance. When the real part of the normalized input impedance (Z_r) approaches 1 and the imaginary part (Z_i) approaches 0, the absorber is impedance-matched to free space and reflection is minimized (i.e., absorption is maximized). Therefore, achieving precise impedance matching is essential for high-performance absorption.

Fig. 9(a), 9(b) and 9(c) show the frequency-dependent input impedance of Sr–Ni W-type ferrite absorbers with different W-type ferrite contents. For the 60 wt% absorber, Z_i is close to 0 in the 42–48 GHz range (corresponding to the FMR region), but Z_r remains significantly different from 1, indicating imperfect impedance matching. Consequently, the RL remained above –10 dB, and the EAB was relatively narrow. However, as the ferrite content increases, Z_i remains near 0 while Z_r moves toward 1, and a relatively broader EAB is achieved. This contrast highlights the critical role of filler loading as an extrinsic tuning parameter. As the ferrite content increases, the composite's overall effective permittivity and permeability values are adjusted. While the $Z_i \sim 0$ condition is maintained across the FMR band (enabled by the intrinsic magnetic loss), the Z_r value is shifted closer to the ideal value of 1. The 80 wt% absorber (Fig. 9(c)) represents the optimal concentration where $Z_r \sim 1$ and $Z_i \sim 0$ are satisfied simultaneously at 48.8 GHz. This near-ideal matching of both conditions produces RL below –40 dB (> 99.99% absorption).

To validate the impedance-matching analysis, the calculated RL spectra were compared with one-port S-parameter (S_{11}) measurements of 80 wt% absorber backed by a copper plate. The measured sample had a thickness of 0.65 mm, identical to the value used in the calculations. As shown in Fig. 9(d), the calculated and measured RL spectra are in good agreement, supporting the impedance-matching interpretation.

Finally, the 80 wt% absorber achieved a wide EAB of 9.3 GHz (40.9-50.2 GHz) at 0.65 mm thickness. These results demonstrate that Sr–Ni W-type ferrite is an effective EM wave absorber dominated by FMR-driven magnetic loss, and that simultaneous matching of both real and imaginary parts of the input impedance achieved through optimization of filler content is essential for superior absorption performance.

4. Conclusion

Optimized processing conditions for the reliable synthesis of single-phase Sr–Ni W-type ferrite via a coprecipitation route were established, and the resulting W-type ferrite powders were incorporated into thermoplastic polyurethane (TPU) to design flexible electromagnetic wave absorbers. Systematic analysis of precipitant composition and calcination temperature showed that a NaOH-Na_2CO_3 mixed precipitant combined with calcination at 1250 °C yields the most favorable conditions for single-phase W-type formation. The W-type ferrite powders were mixed into TPU at various powder loadings, and reflection loss (RL) was evaluated using transmission-line theory. At 80 wt% W-type ferrite loading and 0.65 mm thickness, the absorber achieved a wide effective absorption bandwidth (EAB) of ~9.3 GHz, demonstrating high absorption performance at minimal thickness. The production of single-phase W-type ferrite without detectable secondary phases under these processing conditions, providing a robust basis for reproducible absorber performance and enhances the material's practicality for high-frequency applications such as EMI shielding and radar absorbers.

Acknowledgements

This research was supported by the Fundamental Research Program of the Korea Institute of Materials Science (PNKA560) and the Technology Innovation Program (200250804) funded by the Ministry of Trade, Industry & Energy (MOTIE, Korea).

References

[1] H. Shokri-Ghadikolaei, C. Fischione, G. Fodor, P. Popovski, and M. Zorzi, IEEE Trans. Commun. **63**, 3437 (2015).

[2] B. Yan and I. P. Roberts, Electronics **14**, 1436 (2025).

[3] D. D. L. Chung, Mater. Chem. Phys. **255**, 123587 (2020).

[4] N. Trabelsi, L. Chaari Fourati, and C. S. Chen, Comput. Netw. **239**, 110163 (2024).

[5] N.K. Nguyen, D. Kim, V.Q. Phan, M. Kim, P. Park, and J. Nah, Carbon **238**, 120276 (2025).

[6] B. Park, S. Hwang, H. Lee, Y. Jung, T. Kim, S. J. Kwon, D. Jung, and S. B. Lee, Adv. Funct. Mater. **34**, 2406197 (2024).

[7] M. Zahid, S. Siddique, R. Anum, M. F. Shakir, Y. Nawab, and Z. A. Rehan, J. Supercond. Nov. Magn. **34**, 1019 (2021).

[8] A. Li, A. Mehmood, A. Majeed, A. Ahmad, J. Rehman, Q. Peng, S. R. Ejaz, L. Ali, and M. A. Khan, Ceram. Int. **51**, 45378 (2025).

[9] S.-M. Lee, T.-W. Lee, and Y.-M. Kang, J. Alloys Compd. **962**, 171060 (2023).

[10] G. R. Gordani, M. Mohseni, A. Ghasemi, and S. R. Hosseini, Mater. Res. Bull. **76**, 187 (2016).

[11] C. Stergiou and G. Litsardakis, J. Magn. Magn. Mater. **323**, 2362 (2011).

[12] N. Langhof, D. Seifert, M. Göbbels, and J. Töpfer, J. Solid State Chem. **182**, 2409 (2009).

[13] R. C. Pullar, Prog. Mater. Sci. **57**, 1191 (2012).

[14] M. M. Hessien, M. M. Rashad, and K. El-Barawy, J. Magn. Magn. Mater. **320**, 336 (2008).

[15] M. Soroka, J. Buršík, R. Kužel, J. Prokleška, and M. H. Aguirre, Thin Solid Films. **726**, 138670 (2021).

[16] Z. H. Yang, Z. W. Li, and Y. H. Yang, Mater. Chem. Phys. **144**, 568 (2014).

[17] M. Ahmad, I. Ali, F. Aen, M. U. Islam, M. N. Ashiq, S. Atiq, W. Ahmad, and M. U. Rana, Ceram. Int. **38**, 1267 (2012).

[18] E. Ciliberto, G. G. Condorelli, S. La Delfa, and E. Viscuso, Appl. Phys. A **92**, 137 (2008).

[19] I. Szczygieł, K. Winiarska, and A. Sobianowska-Turek, J. Therm. Anal. Calorim. **134**, 51 (2018).

[20] A. Kumar and K. M. Gangawane, Powder Technol. **401**, 117298 (2022).

[21] S. J. Salih and W. M. Mahmood, Heliyon. **9**, e16601 (2023).

[22] Y. Zhang, C. Jia, Q. Wang, Q. Kong, G. Chen, H. Guan, and C. Dong, Nanomaterials. **9**, 1059 (2019).

[23] S. Anand and S. Pauline, Adv. Mater. Interfaces. **8**, 2001810 (2020).

[24] P. Samoila, C. Cojocaru, I. Cretescu, C. D. Stan, V. Nica, L. Sacarescu, and V. Harabagiu, J. Nanomater. **2015**, 713802 (2015).

[25] S. J. Cheon, J. R. Choi, S.-B. Lee, J. I. Lee, and H. Lee, J. Alloys Compd. **976**, 173019 (2024).

[26] S. K. Godara, V. Kaur, S. B. Narang, G. Singh, M. Singh, G. R. Bhadu, J. C. Chaudhari, P. D. Babu, and A. K. Sood, J. Asian Ceram. Soc. **9**, 686 (2021).

[27] H.-S. Cho and S.-S. Kim, Ceram. Int. **45**, 9406 (2019).

[28] C. H. Chen, S. Kodat, M. H. Walmer, S. F. Cheng, M. A. Willard, and V. G. Harris, J. Appl. Phys. **93**, 7966 (2003).